Vortex Influence on Oscillating Airfoils at High Angle of Attack

D. Favier,* C. Maresca,† A. Castex,‡ and C. Barbi§
Institut de Mécanique des Fluides, C N R S, Marseille, France

The influence of a streamwise vortical flow on an oscillating airfoil is investigated in a low subsonic wind tunnel. It constitutes a limiting case of more complex practical flow configurations encountered, for instance, on a rotating helicopter blade section interacting with the vortical wakes generated upstream by the blade tips. The present experimental simulation is realized by means of a semispan airfoil generating a tip vortex convected downstream and nearby the lower side of a second airfoil, which spans the entire test section and oscillates in fore-and-aft motion. Steady and unsteady behavior is obtained from lift, drag, and pitching-moment measurements, and chordwise pressure and skin-friction distributions are performed on the oscillating airfoil. Particular attention is given to the interaction effect of the lifting surface on the path and strength of the impinging vortex.

Nomenclature

A = amplitude oscillation of R, m
a = distance between the torsion dynamometer axis and the test-section wall, m
c = airfoil chord of E and R, m
C_D = drag coefficient, $= D/\frac{1}{2}\rho V_\infty^2 Hc$
C_L = lift coefficient, $= L/\frac{1}{2}\rho V_\infty^2 Hc$
C_M = pitching-moment coefficient, $= M/\frac{1}{2}\rho V_\infty^2 Hc^2$
C_p = pressure coefficient, $= (p-p_\infty)/\frac{1}{2}\rho V_\infty$
d = distance between the test-section centerline and the spanwise point of application of F, m
D,L = drag and lift forces, N
f,ω = frequency and pulsation oscillation of R, Hz and rad/s
F = aerodynamic force acting on R, N
h = airfoil span of E, m
H = airfoil span of R or wind-tunnel height, m
k,λ = reduced frequency and amplitude parameters; $k = c\omega/2V_\infty, \lambda = A\omega/V_\infty$
$L1,L2$ = longitudinal and transversal distance between E and R airfoil, m (see Fig. 1)
M = pitching moment around the quarter chord, Nm
$OXYZ$ = coordinate system defined in Fig. 2
p,p_∞ = static pressure on R or at infinity, Pa
r = radius of integration contour, mm
Re_c = Reynolds number, $= V_\infty c/\nu$
t = time
U,V,W = velocity components defined in Fig. 2, m/s
V_∞ = freestream velocity, m/s
z = spanwise distance between the bottom of the wing and the point of application of F, m
α_R = geometric incidence of R, deg
α_{ss},α_{ds} = incidences for static and dynamic stall, deg
$\Gamma a,\Gamma$ = bounded circulation on the semispan airfoil or vortex strength, m^2/s
ν,ρ = kinematic viscosity and air density, respectively
τ,τ_{st} = unsteady and steady shear stress on R
ωt = phase within the period, deg

Superscript

$(\bar{\ })$ = mean value over the period

Subscripts

E,R = emitting or trailing airfoil
st = steady conditions (R at rest)
t = streamwise vortex

Introduction

IN various practical flow configurations, the interaction phenomena between organized vortices and lifting surfaces play a major role in unsteady three-dimensional aerodynamics. A few examples are given by the vortical flows generated on turbomachine blades, helicopter rotors, and propellers, where the performance prediction is linked with the correct modeling of such interaction effects.

When focusing on the helicopter rotor environment, different types of blade-vortex interactions can be exemplified according to different vortex system orientations. The dynamic stall of retreating blade sections produces spanwise vortices of axes nearly parallel to the blade span, whereas the blade tips generate streamwise vortices of axes nearly perpendicular to the blade span. Due to their relevance for modeling the local aerodynamic characteristics and the overall rotor performance, in recent years these basic spanwise and streamwise blade-vortex interactions have given rise to active research, including theoretical and experimental studies.[1-13]

The influence of blade-vortex interactions on the rotor blade loading has been demonstrated numerically by recent two- and three-dimensional calculation models in transonic flows.[1,2] Panel methods[3] as well as discrete vortex techniques[4,5] have also been used for the problem of a convecting vortex interacting with a stationary airfoil in a subsonic uniform flow. Some studies have reported on vortex stability[4] and finite core's influence[5] on the distortion of the vortex path.

The aforementioned interaction configurations occurring on the rotor blade have also been experimentally studied by means of simplified two- and three-dimensional unsteady flow simulations. The case of airfoil/spanwise vortex interaction has been investigated in two-dimensional unsteady simulations, where the vortical wake flow is generated either from the dynamic stall of pitching[6] and translating[7,8] airfoils or from stationary cylinders.[9] The vortical wake interacts with a second stationary airfoil set downstream at different longitudinal and lateral positions. In these studies, the unsteady effects observed on the stationary airfoil are shown

Presented as Paper 86-1837 at the AIAA 4th Applied Aerodynamics Conference, San Diego, CA, June 9-11, 1986; received July 21, 1986; revision received Feb. 18, 1987.

*CNRS Research Scientist. Member AIAA.
†CNRS Senior Research Scientist. Member AIAA.
‡IMFM Graduate Student.
§CNRS Research Scientist.

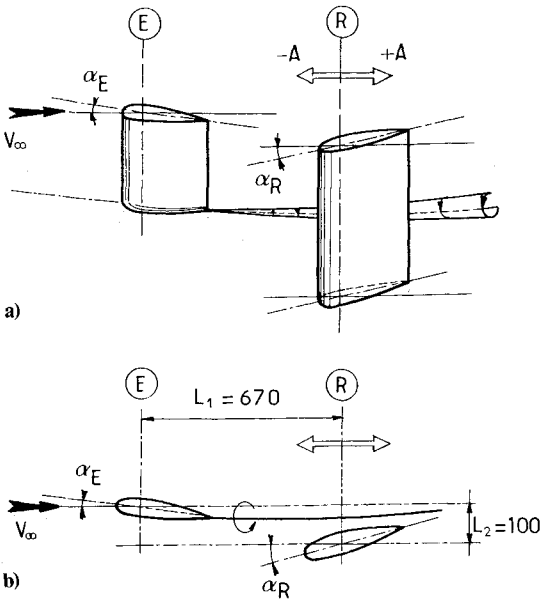

Fig. 1 Simulation of basic airfoil-streamwise vortex interaction: a) side view, b) top view.

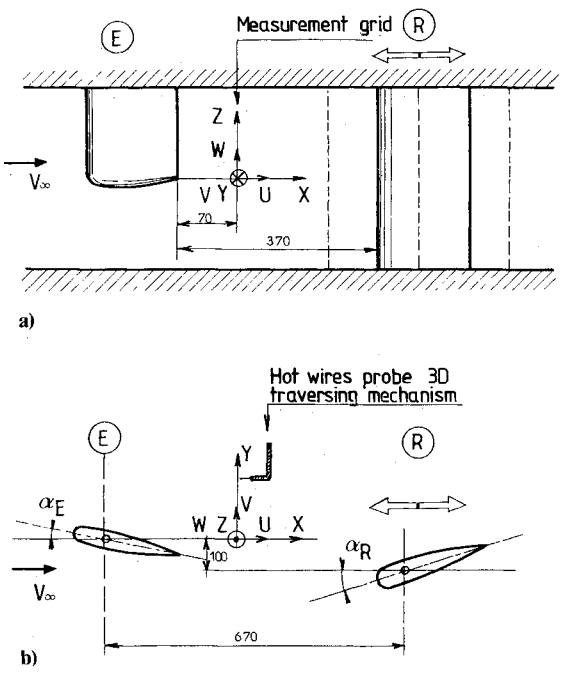

Fig. 2 Coodinates system and *U, V, W*, velocity components: a) side view, b) top view.

to be strongly dependent on the vortex strength[9] as well as on the simultaneous fluctuations of velocity and incidence[6-8] produced by the periodic impinging vortical wake.

In most experimental studies undertaken for simulating the airfoil/streamwise vortex interaction,[10-12] the basic problem has been considered in steady conditions by means of semispan airfoils at rest in a three-dimensional flow configuration. Very few experiments[13] have indeed considered unsteady flow conditions where the interacted airfoil is oscillating or rotating. In Ref. 13, the experimental simulation is realized by setting a vortex generator upstream of a nonlifting rotor. Chordwise pressure distributions have been measured on the surface of the interacted blade sections, but only at the forward azimuthal blade position ($\psi = 180$ deg), where the vortex axis is nearly parallel to the blade span.

Moreover, in these previous studies some aspects of the basic airfoil/streamwise vortex interaction problem have not been sufficiently addressed and still require additional experimental data to support and improve the theoretical models. Specifically, those aspects concern the airfoil's influence on both the path and intensity of the vortex as well as the interaction effects on the behavior of the airfoil forces and moments.

In the present investigation, some of these questions are addressed by considering a streamwise vortical flow generated by a first stationary semispan airfoil interacting with a second airfoil that oscillates in fore-and-aft motion in order to simulate the cyclic velocity fluctuations encountered by a given blade section during the rotation.

In the following sections, particular attention is given to the determination of modifications of the vortex path and intensity due to the oscillating airfoil. To this end, a detailed hot-wire survey through the vortex core is carried out. Then, the complete aerodynamic behavior of the interacted airfoil set at low and high angles of attack is deduced from overall measurements (C_L, C_D, C_M) and from local measurements of pressure and skin friction along the airfoil surface.

Experimental Facilities and Measurement Procedures

A study was conducted in the low subsonic open circuit wind tunnel at the Institut de Mécanique des Fluides (IMFM) (rectangular test section: 0.5×1 m^2; length, 3 m; velocity: 2.5-25 m/s). The basis interaction problem is simulated by means of the three-dimensional flow configuration depicted in Fig. 1.

The vortical flow is generated by placing a semispan airfoil (E) (NACA 0012 profile; $c = 0.30$ m; $h = 0.32$ m) at incidence $\alpha_E = 6$ deg in the uniform flow. On the last 5% of the wingspan the lateral wedge is rounded (elliptical cross section along the spanwise direction, and NACA 0012 planform profile in the chordwise direction), in order to produce a tip vortex axis nearly parallel to the main flow direction (see Fig. 1).

A second airfoil (R) spanning vertically the entire test section (NACA 0012 profile; $c = 0.30$ m; $h = 0.50$ m) is attached to a frame oscillating in longitudinal motion parallel to the freestream direction (see Fig. 1a). The mechanical drive[14,15] is designed to fit beneath the test section and to produce a pure sinusoidal motion ($X = -A \sin \omega t$), where the amplitude A and frequency f can be varied in the following ranges: 0.04 m $\leq A \leq$ 0.17 m, 0.5 Hz $\leq f \leq$ 6 Hz.

As shown in Fig. 1b, the relative position of E and R ($L_1 = 670$ mm and $L_2 = 100$ mm when R is at rest or at $\omega t = 0$ deg) is selected so that the tip vortex is passing along and nearby the lower side of R. In the present investigation, the following test conditions are fixed: $\alpha_E = 6$ deg, $V_\infty = 5.1$ m/s, $A = 0.17$ m, and $f = 2.5$ Hz, while the incidence of the trailing airfoil R can be varied from -25 to 25 deg (positive incidence corresponds to $Y > 0$, as shown in Fig. 2).

A hot-wire probe (DISA 55R51) mounted on a three-dimensional device was used to determine the three-dimensional velocity field in a transversal plane located at $X = 70$ mm downstream of the trailing edge of E, as shown in Fig. 2. In this plane, $X_t = \text{const}$, the vortex center location (Y_t, Z_t) is then deduced from the U, V, W velocity survey along the Y and Z directions. The point (X_t, Y_t, Z_t) of vortical flow where the condition $V = W = 0$ is reached has been defined as the vortex center position.

From this vortex center location, the square measurement grid (40×40 mm^2) is composed of 121 points distributed along the Y, Z axis with a mesh size $\Delta Y = \Delta Z = 4$ mm. A precise characterization of the vortex strength and displacement is then deduced from the radial velocity component $V_r = (V^2 + W^2)^{1/2}$ as obtained in each of the 121 measuring points.

Chordwise distributions of static pressure and skin friction are measured by miniature sensors[7,8] mounted flush on the R

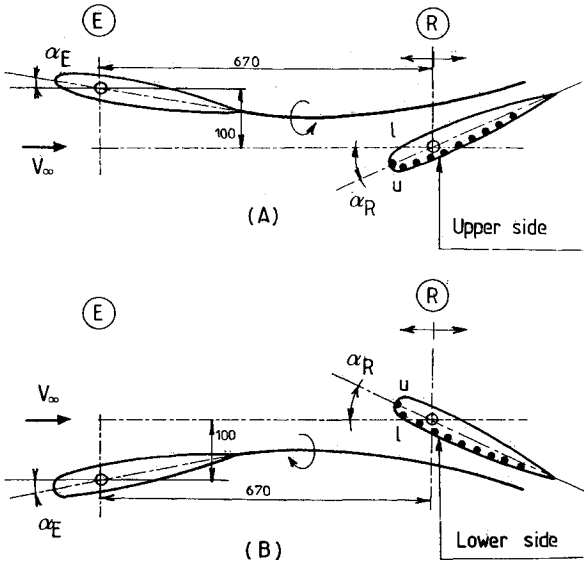

Fig. 3 Symmetrical flow configurations for pressure measurements: a) upper side, b) lower side.

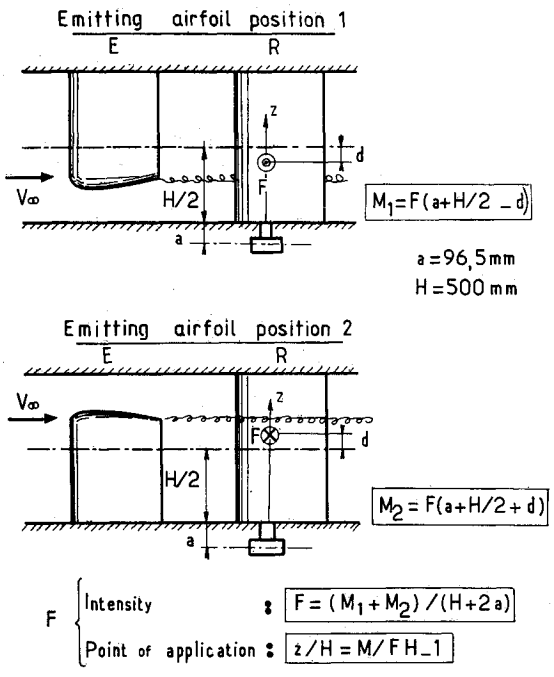

Fig. 4 Force measurement principle.

airfoil surface and bonded to the initial skin along the midspan section ($z/h=0.5$) of the trailing airfoil.

Two models of the same trailing wing have been equipped with 10 pressure transducers (ENDEVCO 8507-2) located at $x/c=0$, 0.04, 0.12, 0.20, 0.30, 0.40, 0.50, 0.60, 0.70, 0.80, and with nine hot-film gages located at the same chordwise abscissa (except $x/c=0$). Only one side of the wing has been instrumented in the midspan section. As shown in Fig. 3, the upper- and lower-side distributions are obtained by generating two symmetrical flow configurations [by changing the incidence values (α_E, $-\alpha_R$) in ($-\alpha_E$, α_R) and exchanging transversal positions of E and R].

Measurements of overall forces and pitching moment are carried out using statically and dynamically calibrated torsion dynamometers.[14,15] In the present three-dimensional flow configuration and for the symmetrical NACA 0012 airfoil, the force measurement principle is based on two successive moment measurements (M_1, M_2), as illustrated in Fig. 4.

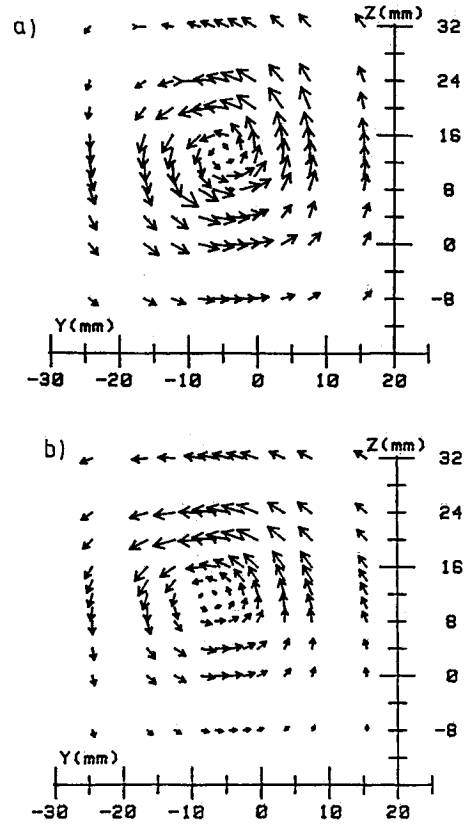

Fig. 5 Mean radial velocity field V_r for $\alpha_R=20$ deg and $V_\infty=5.1$ m/s: a) steady flow, b) unsteady mean flow.

The emitting semispan airfoil E is first mounted on the upper wall of the test section (position 1 in Fig. 4), and the torsion dynamometer located at the distance a under the test-section floor gives the moment as

$$M_1=F(a+H/2-d) \tag{1}$$

where a represents the distance between the torsion dynamometer axis and the test-section floor.

A second measurement of the moment is then made when the semispan airfoil E is mounted on the lower wall of the test section (position 2 in Fig. 4), which gives

$$M_2=F(a+H/2+d) \tag{2}$$

From these two successive measurements, the force intensity and its point of application along the z spanwise direction are obtained from Eqs. (1) and (2) as

$$F=(M_1+M_2)/(H+2a), \quad z/H=(M/FH)-1 \tag{3}$$

where M is defined as $M=(M_1+M_2)/2$.

Note that the symmetrical positions 1 and 2 of E correspond to identical flow configurations on R (due to the change in the rotation sense of the vortex).

Using this technique, the lift and drag components are obtained by placing the torsion dynamometer axis either parallel or normal to the freestream direction. Whereas the pitching moment around the quarter chord is obtained by placing the torsion dynamomenter axis parallel to the wingspan.

Moreover, all the output signals from the torsion dynamometers, hot wires, skin-friction gages, and pressure transducers were digitized IN-110). These data are then harmonically analyzed within a computer to yield the time-averaged value and the four Fourier harmonics in the follow-

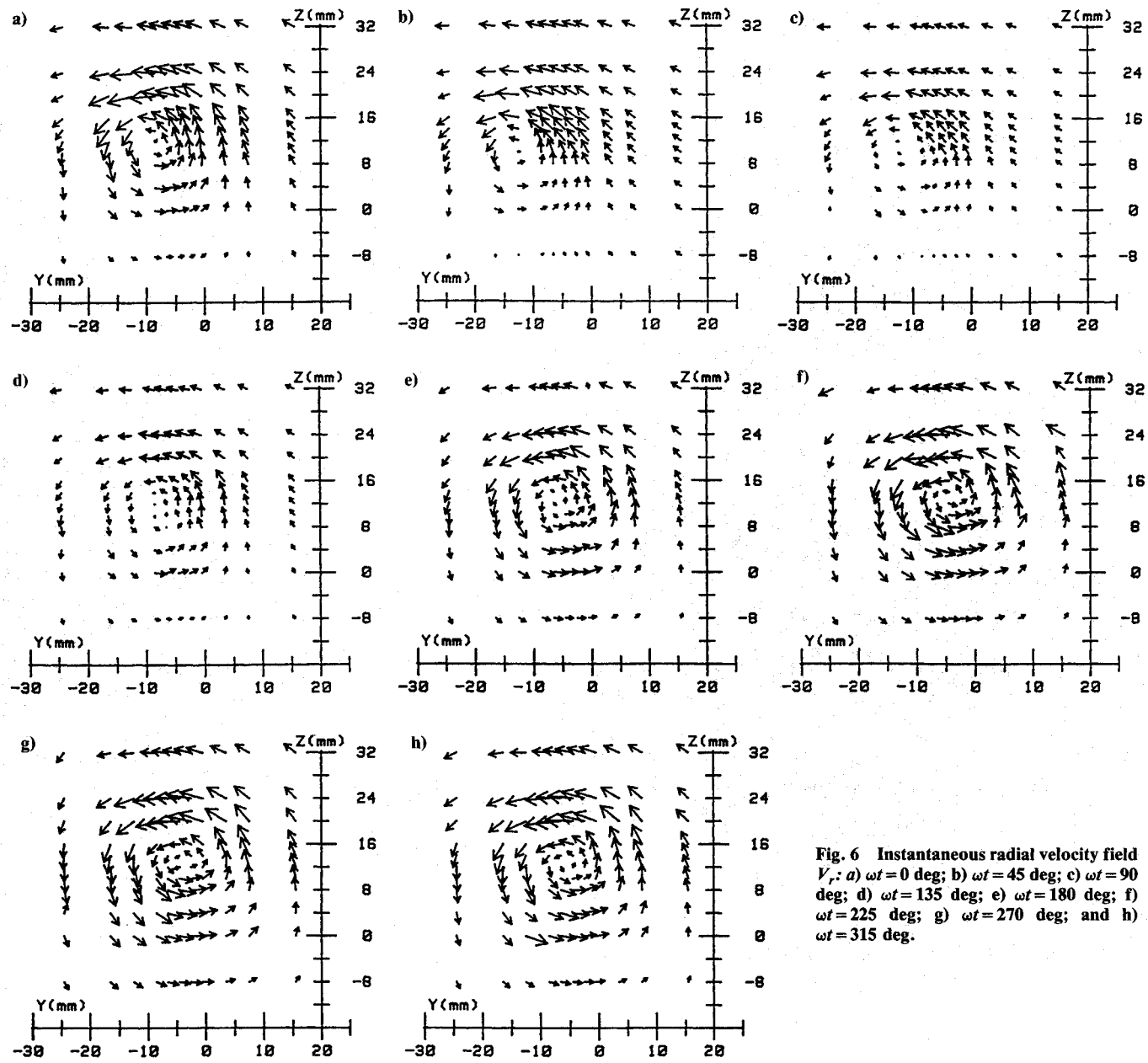

Fig. 6 Instantaneous radial velocity field V_r: a) $\omega t = 0$ deg; b) $\omega t = 45$ deg; c) $\omega t = 90$ deg; d) $\omega t = 135$ deg; e) $\omega t = 180$ deg; f) $\omega t = 225$ deg; g) $\omega t = 270$ deg; and h) $\omega t = 315$ deg.

ing form:

$$C = C_0 + \sum_{n=1}^{4} C_n \cos(n\omega t + \Phi_n) \qquad (4)$$

where C is the measured quantity and C_0 its mean value over a period of oscillation of R.

Influence of the Oscillating Airfoil on the Impinging Vortex

In order to discuss this airfoil's influence, three flow conditions behind E are considered: 1) without R (referred to as the isolated airfoil configuration); 2) with R present but at rest (referred to as the steady flow configuration); 3) with R oscillating in fore-and-aft motion (referred to as the unsteady flow configuration). In each flow configuration the vortex center location is determined, and the radial velocity V_r is measured along the 121 grid points, as previously described. Figure 5 presents the steady velocity field and the unsteady mean velocity field over the period so obtained along the measuring grid. The results indicate only a slight difference between steady and unsteady mean configurations for both the vortex core position and the vortex imprint in the X_t plane considered.

However, when considering the instantaneous radial velocity field at different phases of the period (Figs. 6), it is clear that the airfoil's influence becomes more accentuated than revealed by the mean values. As a function of time, the results exhibit a distortion of the velocity field and a vortex center excursion. This influence appears to be maximum for 0 deg $\leq \omega t \leq$ 90 deg when R is moving along the $-X$ direction. At $\omega t = 270$ deg (Fig. 6g), both the velocity field and the vortex center position are similar to steady conditions, and R is then reaching its maximum backward position in the X direction.

The time-dependent displacement of the vortex center in the YZ plane is plotted in Fig. 7 for the same eight phase values as in Fig. 6. Also shown in the figure are the isolated airfoil case (without R) and the steady and unsteady mean cases. The instantaneous excursion loop of the vortex center indicates that the amplitude of fluctuation is about 2 mm in the Z direction, whereas it reaches 7 mm in the Y direction. Starting from $\omega t = 0$ deg (point 1 in Fig. 7), the Y coordinate rapidly decreases as R is moving forward, then the vortex comes closer to the R surface (0 deg $\leq \omega t \leq$ 90 deg, points 2 and 3) and goes back to a position close to the steady one as R moves backward (90 deg $\leq \omega t \leq$ 270 deg, points 4–6). In the present tests, the YZ plane is fixed and R oscillates; however, some

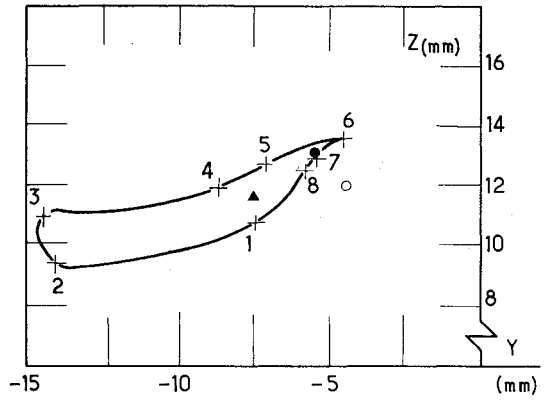

Pts	1	2	3	4	5	6	7	8
ωt	0°	45°	90°	135°	180°	225°	270°	315°

Fig. 7 Steady, unsteady mean and instantaneous vortex center positions (Y_t, Z_t) in the the plane X_t = 70 mm downstream of the trailing edge of E.

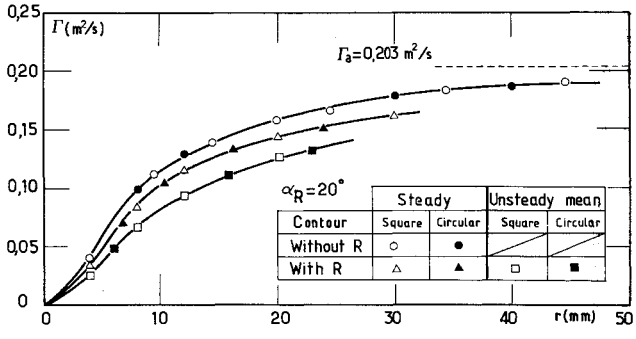

Fig. 8 Mean and unsteady mean vortex strengths.

evidence of such unsteady behavior of the vortex center (attracted during the R forward motion and pressed back during the R backward motion) can be found in the flow visualizations of Ref. 12 by considering a quasisteady displacement of R near the curved vortex line.

From the radial velocity measurements in Figs. 5 and 6, the vortex strength Γ has also been determined by integrating V_r along a closed contour ($\Gamma = \oint V_r ds$) including the vortex core. The integrations have been performed along either a square contour (r side varying from 4 to 40 mm) or a circular contour (r radius also varying in the same range). As a function of the integration contour size (square or circular), the vortex strength is plotted in Fig. 8 for isolated steady and unsteady mean flow configurations.

First, it can be noticed in Fig. 8 that the values of Γ are independent of the shape integration contour (square and circular contours give points fitting on the same curve). Moreover, the plot corresponding to the isolated airfoil case (without R) shows that the vortex intensity Γ increases with the contour size r, and has an asymptotic value of about 0.195 m²/s. This value represents 96% of the maximum bound circulation Γ_a on the semispan airfoil (Γ_a = 0.203 m²/s). This value of Γ_a is obtained from $\Gamma_a = C_L V_\infty c/2$ and from lift measurement on E in uniform flow (V_∞ = 5.1 m/s, α_E = 6 deg) by the torsion dynamometer technique (C_L = 0.265 at α_E = 6 deg). The two other curves of Fig. 8 clearly show that the presence of R (either at rest or oscillating) induces a drop of

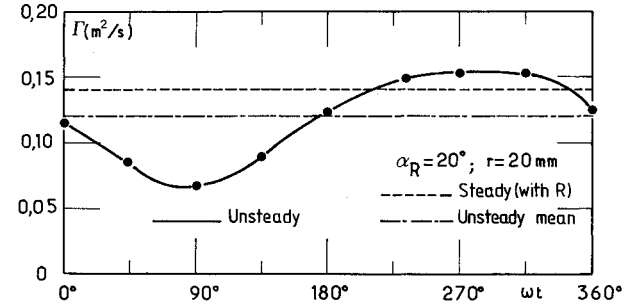

Fig. 9 Instantaneous vortex strength variations as a function of time $\Gamma = \Gamma(\omega t)$.

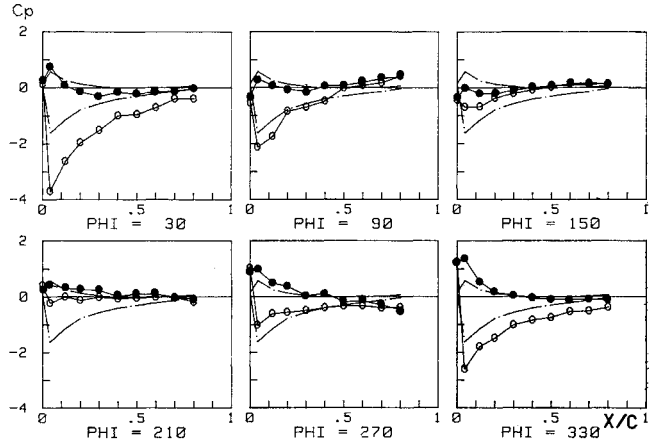

Fig. 10 C_p distributions on R at α_R = 6 deg: unsteady flow:- ○ - upper side; - ● - lower side; steady flow: -·-.

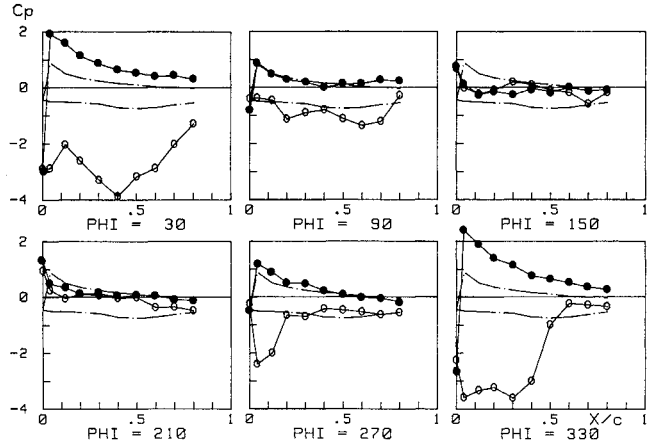

Fig. 11 C_p distributions on R at α_R = 20 deg: unsteady flow:- ○ - upper side; - ● - lower side; steady flow: -·-.

the vortex strength. In these cases, the asymptotic value of Γ reaches only 90 and 84% of Γ_a, respectively, for steady flow (with R) and unsteady mean flow configurations.

In order to obtain the vortex strength behavior as a function of time, integrations of the instantaneous velocity fields have been made for each of the eight phase values of Fig. 6, with a contour r = 20 mm. Figure 9 shows the instantaneous evolution $\Gamma = \Gamma(\omega t)$ so obtained, as well as the corresponding levels of Γ for steady flow (with R) and unsteady mean flow configurations. Near ωt = 270 deg, the instantaneous Γ becomes maximum and slightly exceeds the steady flow level. This should be related to the previous statement of a flowfield at ωt = 270 deg similar to the steady flow conditions. Moreover, when R moves forward (0 deg ≤ ωt ≤ 90 deg and 270 deg ≤ ωt ≤ 360 deg), the results indicate a decrease of the vortex in-

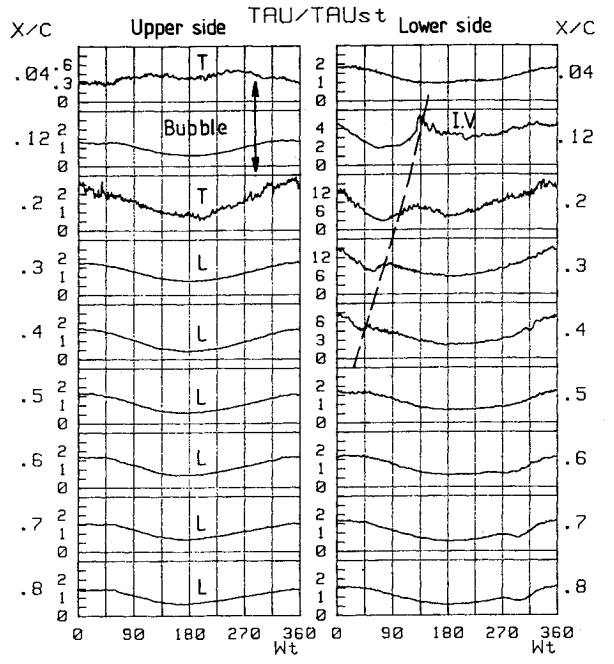

Fig. 12 Skin-friction waveforms on R at $\alpha_R = 6$ deg (I.V. = impinging vortex; L = laminar; T = turbulent).

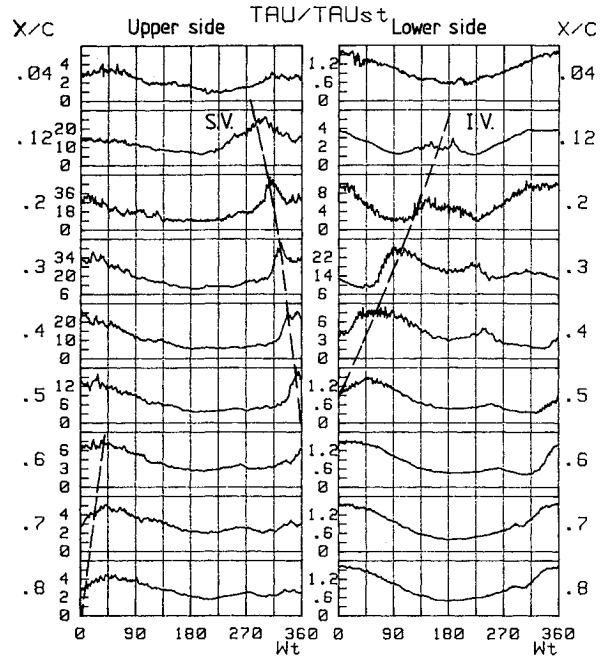

Fig. 13 Skin-friction waveforms on R at $\alpha_R = 20$ deg (I.V. = impinging vortex; S.V. = stall vortex).

tensity as the vortex deviates from its steady position and comes closer to R (see Fig. 7).

This study of the airfoil's influence on the streamwise vortex reveals typical features on both the vortex path and strength that should be included in any attempt at calculating the unsteady airfoil–streamwise vortex interacting effects.

Unsteady Aerodynamic Behavior of the Interacted Airfoil

For $\alpha_R = 6$ and 20 deg, local measurements of C_p on the upper and lower sides along the midspan section of R are presented in Figs. 10 and 11 for different phase values of the period. The unsteady distributions are compared to corresponding steady ones.

The unsteady C_p distributions of the interacted airfoil show an overshoot on the unsteady upper-side distribution for 330 deg $\leq \omega t \leq$ 90 deg + 360 deg (Figs. 10 and 11) that is particularly strong at high angle of attack (Fig. 11).

The C_p values for 150 deg $\leq \omega t \leq$ 210 deg are below the steady level. In Fig. 11, the steady pressure measurements reveal the presence of a separated flow on the upper side of R.

All these pressure unsteady effects feature the dynamic stall generated by velocity variations.[14] Although the C_p distributions on the lower side behave as expected under velocity fluctuations, the suction phenomenon, produced by the impinging vortex passing by the airfoil, reduces the pressure on this side. Figure 10 gives evidence of this effect at $\alpha_R = 6$ deg, whereas at $\alpha_R = 20$ deg the large pressure fluctuations due to stall tend to mask the interacting vortex influence.

In complement of pressure distributions, skin-friction measurements demonstrate clearly the impinging vortex propagation along the lower side of R, as shown in Figs. 12 and 13 ($\alpha_R = 6$ and 20 deg, respectively). At each sensor chordwise location, the unsteady skin friction has been scaled by the steady value measured with R at rest.

The vortex signature is detected on these records by a slight decrease followed by a fluctuating signal of higher level. For both cases considered (6 and 20 deg), the signature of the impinging vortex along the chord (annotated "I.V." in Figs. 12 and 13) is located at $0.12 \leq x/c \leq 0.5$ for phases varying between 150 and 30 deg. The upper-side records, at $\alpha_R = 6$ deg, reveal the presence of a leading-edge bubble (see laminar and turbulent levels of the fluctuating upper-side signal, noted "L" and "T" in Fig. 12), which extends from $x/c = 0.04$ to $x/c = 0.20$.

In Fig. 13, $\alpha_R = 20$ deg, the upper-side skin-friction waveforms show that the propagation velocity of the vortex generated during stall can be evaluated at $V_t = 0.43 V_\infty$. Similar results on velocity propagation have already been obtained on an isolated oscillating airfoil[14] ($V_t \simeq 0.5 V_\infty$). A detailed unsteady aerodynamic coefficients behavior of the interacted airfoil is presented in Figs. 14 and 15, respectively, for $\alpha_R = 6$ and 20 deg. The C_L, C_D, and C_M coefficients and the spanwise variation of z/H are plotted versus ωt. The corresponding steady levels are represented as dotted lines.

At low incidence, $\alpha_R = 6$ deg, the coefficients C_L and C_D reach their maxima when the relative velocity due to the airfoil motion is nearly about its maximum (phase lag less than 20 deg).

In Fig. 15, $\alpha_R = 20$ deg, the magnitude of the overshoot on unsteady values is significant on the three components. This is the result of the cyclic separation and reattachment process of the boundary layer on the upper side of R (Figs. 11 and 13).

In fact, similar unsteady features are obtained in the case of an isolated oscillating airfoil and are to be connected[14,15] with the relative velocity variations imposed on R. In the present flow conditions, where the generated vortex strength is relatively weak either in instantaneous or unsteady mean values (see Figs. 8 and 9), the influence of the vortex does not drastically modify the unsteady flowfield around R. This can be seen in Fig. 16, where the steady and unsteady C_M measured on the interacted airfoil are compared with the same quantities corresponding to the isolated oscillating airfoil. Fore-and-aft motion at small angles of attack ($\alpha_R = 6$ deg) induces a strong nose-down moment for $90 \leq \omega t \leq 270$ deg. The interacting vortex increases this effect but also introduces an average phase lag of about 20 deg. This phase lag appears to be more important when passing from nose-down to nose-up moment ($\omega t = 270$ deg) than from nose up to nose down ($\omega t = 90$ deg).

The main influence on the impinging vortex is given in Fig. 16 ($\alpha_R = 6$ deg), where the C_M steady value corresponding to the interacted airfoil changes its sign and becomes positive.

The instantaneous spanwise position of the point of application z/H is presented versus ωt in Figs. 14 and 15. In Fig. 14 ($\alpha_R = 6$ deg), the steady value of z/H is equal to 0.52, the

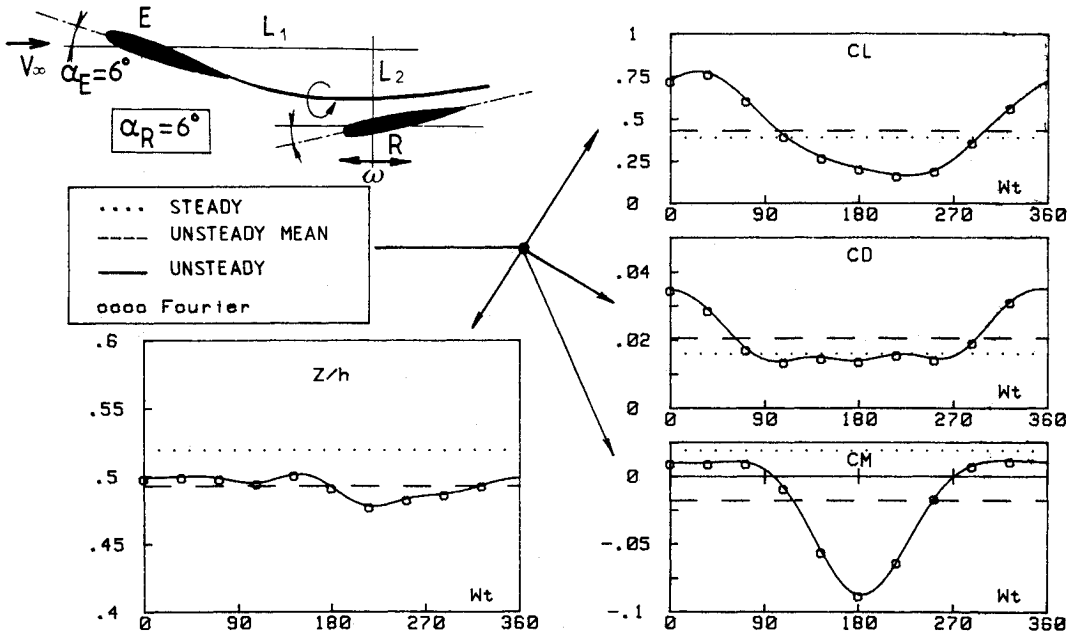

Fig. 14 Instantaneous aerodynamic coefficients on R at $\alpha_R = 6$ deg.

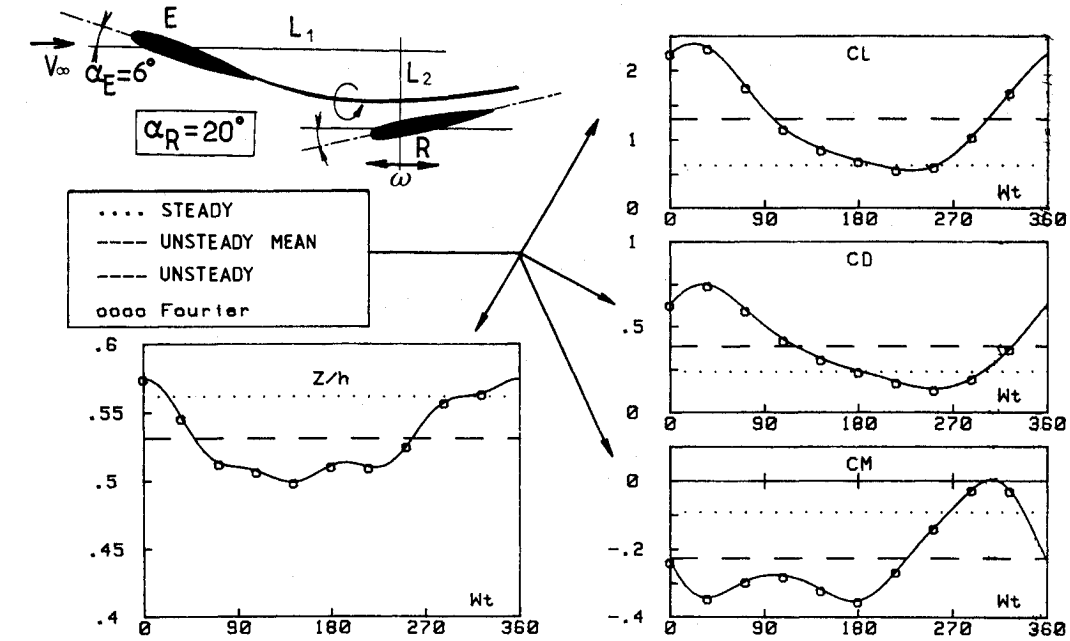

Fig. 15 Instantaneous aerodynamic coefficients on R at $\alpha_R = 20$ deg.

unsteady mean value is close to 0.50, and only small fluctuations are measured around this mean value. In Fig. 15 ($\alpha_R = 20$ deg), the steady value is higher ($z/H = 0.56$), as well as the unsteady mean value ($z/H = 0.53$). The maximum of fluctuations ($z/H = 0.58$) is reduced by 330 deg $\leq \omega t \leq 30 + 360$ deg, when the boundary layer is reattached and when the vortex is generated on the upper side of R. For $\alpha_R = 6$ deg, the point of application moves around the quarter chord from an upstream extreme position of $x/c = 0.22$ (when $\omega t = 90$ and 270 deg) to a downstream position of $x/c = 0.35$ (when $\omega t = 180$ deg). For $\alpha_R = 20$ deg, this point of application is located downstream of the quarter chord, except when 300 deg $\leq \omega t \leq 330$ deg.

These remarks have to be connected with the comments on the instantaneous excursion loop of the vortex center. In Fig. 7, the position of the center of vorticity exhibited slight fluctuations in the Z direction and a maximum of amplitude variations in the Y direction. In the same way, the point of application of the overall force experiences slight variations in the spanwise direction and a maximum displacement amplitude around the quarter chord in the chordwise direction.

The influence of unsteady interaction of the streamwise vortex on the airfoil, previously discussed for the two incidence cases $\alpha_R = 6$ and 20 deg, has been extended to a detailed investigation of the steady and unsteady mean values of C_L, C_D, and C_M over a wide range of α_R varying from 0 to 20 deg.

The lift coefficients $\bar{C}_L$ and C_{Lst} measured on R as a function of α_R, in both the isolated and interacted airfoil configurations, are presented in Fig. 17. The slope $dC_{Lst}/d\alpha_R$ is substantially reduced in the presence of E. The static stall angle α_{ss} is shifted about 1 deg, up to $\alpha_{ss} = 13$ deg. The data obtained on R oscillating when the vortex is present show an increase of the mean lift coefficient $\bar{C}_L$ over a period. As already observed,[14,15] on an isolated airfoil oscillating in fore-and-aft motion, the growth of the mean lift coefficient $\bar{C}_L$ is increased as α_R increases, especially when $\alpha_R > \alpha_{ss}$.

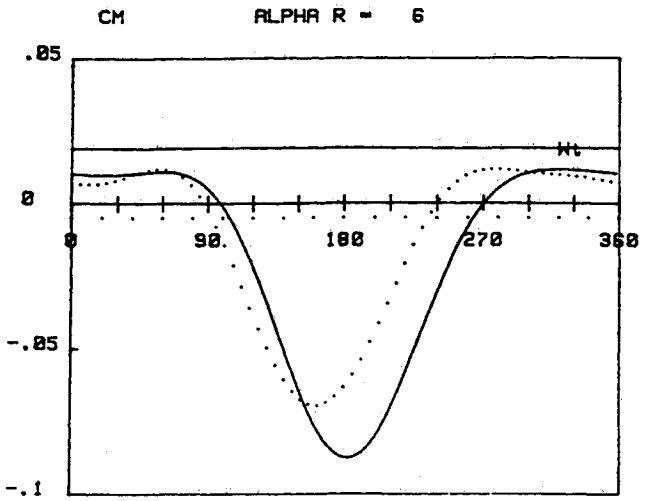

Fig. 16 Steady and unsteady pitching-moment coefficients on *R*: — interacted airfoil; --- isolated airfoil.

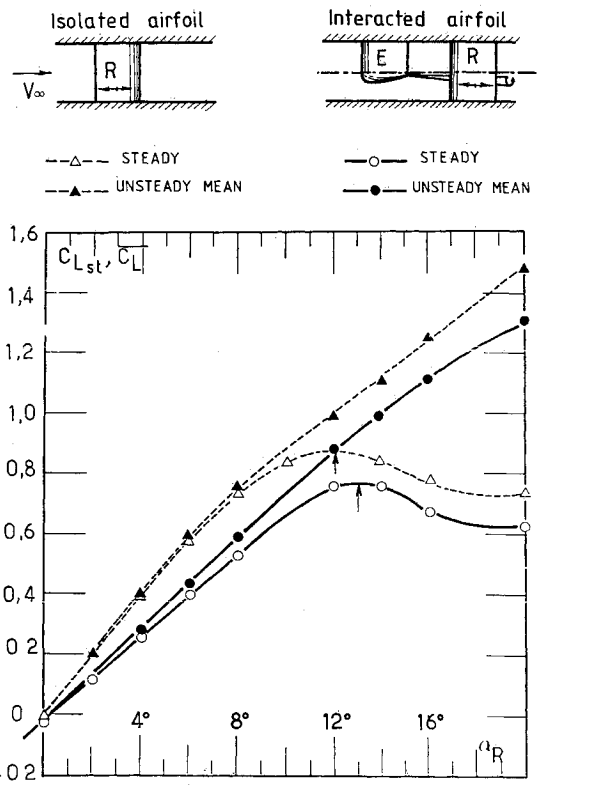

Fig. 17 Steady and unsteady mean coefficient C_L vs α_R, with and without E.

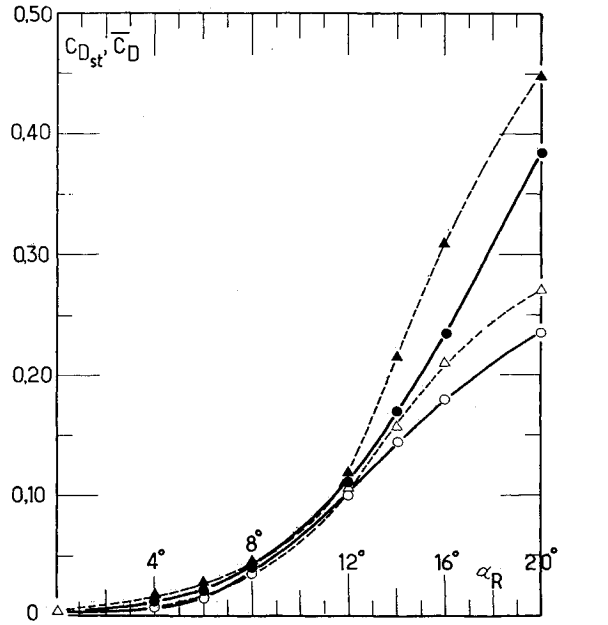

Fig. 18 Steady and unsteady mean coefficient C_D vs α_R, with and without E (see Fig. 17 for symbols).

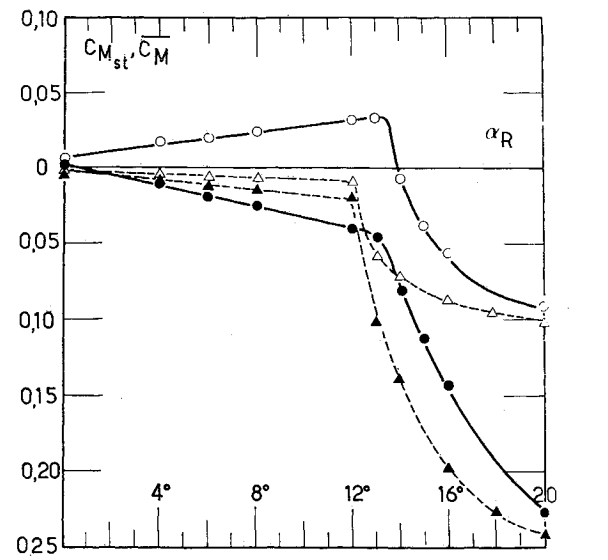

Fig. 19 Steady and unsteady mean coefficient C_M vs α_R, with and without E (see Fig. 17 for symbols).

In Fig. 18, when E is present, the interacted steady drag coefficient C_{Dst} is less than the isolated C_{Dst} for either small ($\alpha_R < 6$ deg) or high ($\alpha_R > 13$ deg) angles of attack. When R oscillates, the unsteady mean drag coefficient $\bar{C}_D$ is substantially increased in both flow configurations, without and with E.

These results well confirm that the unsteady mean trends of $\bar{C}_L$ and $\bar{C}_D$ generated by the fore-and-aft motion of an isolated airfoil are similarly obtained when the oscillating airfoil is interacted by the streamwise vortex. However, it should be noticed that moment coefficient behaviors ($\bar{C}_M$, C_{Mst}) are strongly influenced by the presence of the impinging vortex, as shown in Fig. 19. In steady flow and for $\alpha_R < \alpha_{ss}$, the vortical flow passing by the airfoil R induces a torque (opposite to the experiment without E) that is strong enough to produce a static moment alteration from nose up to nose down. For high angles of attack ($\alpha_R > \alpha_{ss}$), the vortex interaction effect persists but the stall regime keeps the moment coefficient C_{Mst} negative for all values of $\alpha_R > \alpha_{ss}$. At low angles of attack, $\alpha_R < \alpha_{ss}$, the combined effect of velocity variations and vortex influence induces a strong decrease of $\bar{C}_M$, such that $\bar{C}_M$ always remains below the noninteracted values.

In Fig. 20, the unsteady mean quantities $\bar{C}_L$, $\bar{C}_D$, and $\bar{C}_M$ are scaled by the corresponding steady values C_{Lst}, C_{Dst}, and C_{Mst} to obtain a comparative representation of the fore-and-aft motion with and without vortex interaction. As stressed by this figure, for a wide range of α_R, the unsteady mean response of the lifting surface to the vortex influence is primarily obtained on $\bar{C}_M/C_{Mst}$. The moment ratio exhibits a drastic change below stall. It appears to be negative for

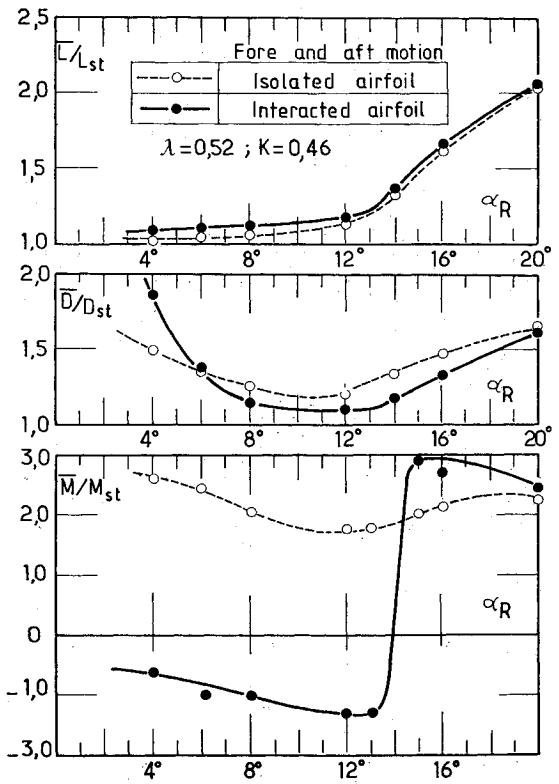

Fig. 20 Unsteady mean effects in fore-and-aft motion with and without vortex interaction.

$\alpha_R < \alpha_{ss}$ and positive for $\alpha_R > \alpha_{ss}$, significantly exceeding the noninteracted values.

Summary and Conclusions

An experimental study has been conducted on the interaction of a streamwise vortex generated by a stationary semispan airfoil, with a fore-and-aft oscillating airfoil set at various geometric angles of attack.

The primary point of interest is the influence of the oscillating airfoil on the vortex path and strength. Results of this investigation indicate that the trapping of the vortex is associated with a decrease in strength during the R forward motion. The vortex is pressed back away from the lower side of the airfoil with an increasing intensity during the R backward motion. These features appear to be significant of the interaction phenomenon and, therefore, should be taken into account in theoretical modeling.

The influence of the streamwise vortex on the trailing airfoil has been studied for $\alpha_R = 6$ and 20 deg from local unsteady distribution pressure and skin friction, as well as from aerodynamic forces and moments measurements. It has been shown that the general trends created by the velocity variations due to airfoil motion are not fundamentally affected by the vortex-induced suction on the lower side of R. The main effect has been observed on the moment coefficient with an increase of amplitude and a shift in phase.

Finally, a systematic comparison between interacted and isolated oscillating airfoils set at different α_R from 0 to 20 deg has been made concerning steady and unsteady mean values of C_L, C_D, and C_M. It has revealed that the vortex influence is primarily obtained on the $\bar{C}_M/C_{Mst}$ ratio. This ratio is negative below stall and changes its sign for $\alpha_R > \alpha_{ss}$, and the unsteady mean values $\bar{C}_M$ significantly exceed the corresponding noninteracted levels.

Acknowledgment

This work was supported by the Service Technique des Programmes Aéronautiques under Grant 84-95005.

References

[1]Srinivasan, G. R., McCroskey, W. J., and Baeder, J. D., "Aerodynamics of Two-Dimensional Blade-Vortex Interaction," AIAA Paper 85-1560, July 1985.

[2]Strawn, R. C. and Tung, C., "The Prediction of Transonic Loading of Advancing Helicopter Rotors," *Proceedings of the AGARD/FDP Symposium on Applications of Computational Fluid Dynamics in Aeronautics*, Paper 7, Aix-en-Provence, France, April 1986, pp. 1-14.

[3]Maskew, B. and Rao, B. M., "Calculation of Vortex Flows on Complex Configurations," *Proceedings of the 13th ICAS-AIAA International Congress of Aeronautical Science,* ICAS Paper 82-623, Aug. 1982, pp. 351a-351f.

[4]Huang, M. K. and Chow, C. Y., "Trapping of a Free Vortex by Joukowski Airfoil," *AIAA Journal,* Vol. 20, March 1982, pp. 292-298.

[5]Panaras, A. G., "Modeling of the Vortex-Airfoil Interaction," *Proceedings of the AGARD-FDP/FMP Symposium on Unsteady Aerodynamics—Fundamentals and Applications to Aircraft Dynamics*, Paper S3, Göttingen, FRG, May 1985, pp. 1-16.

[6]Mathioulakis, D. S., Kim, M. J., Telionis, D. P., and Mook, D. T., "On the Wake of a Pitching Airfoil," AIAA Paper 85-1621, July 1985.

[7]Maresca, C. and Favier, D. "Experimental Study and Modeling of the Influence of a Periodic Wake on a Lifting Surface," AIAA Paper 84-1660, June 1984.

[8]Favier, D., Castex, A., and Maresca, C., "Unsteady Characteristics of an Airfoil Interacting with a Vortical Wake," AIAA Paper 85-1707, July 1985.

[9]Meier, G. E. A. and Timm, R. "Unsteady Vortex Airfoil Interaction," *Proceedings of the AGARD-FDP/FMP Symposium on Unsteady Aerodynamics—Fundamentals and Applications to Aircraft Dynamics*, Paper 16, Göttingen, FRG, May 1985, pp. 1-10.

[10]Ham, N. D., "Some Conclusions from an Investigation of Blade-Vortex Interaction," *Journal of the American Helicopter Society,* Vol. 20, Oct. 1975, pp. 26-31.

[11]Ceroni, P., "Etude expérimentale et théorique d'un tourbillon et de son interaction avec une demi-aile á la paroi," ONERA RT-118/1369 AN, Nov. 1982.

[12]McAllister, K. W. and Tung, C., "Airfoil Interaction with an Impinging Vortex," NASA TP-2273, 1984.

[13]Caradona, F. X., Laub, G. H., and Tung, C., "An Experimental Investigation of the Parallel Blade-Vortex Interaction," *Proceedings of the Tenth European Rotorcraft Forum*, Paper 4, The Hague, the Netherlands, 1984, pp. 1-30.

[14]Maresca, C., Favier, D., and Rebont, J., "Experiments on an Airfoil at High Angle of Incidence in Longitudinal Oscillations," *Journal of Fluid Mechanics,* Vol. 92, Pt. 4, June 1979, pp. 671-690.

[15]Favier, D., Maresca, C., and Rebont, J., "Dynamic Stall Due to Fluctuations of Velocity and Incidence," *AIAA Journal,* Vol. 20, July 1982, pp. 865-871.